

**This is a self-archived version of an original article. This version may differ from the original in pagination and typographic details.**

**Author(s):** Korpelin, Ville; Melander, Marko M.; Honkala, Karoliina

**Title:** Reducing the Irreducible : Dispersed Metal Atoms Facilitate Reduction of Irreducible Oxides

**Year:** 2022

**Version:** Published version

**Copyright:** © 2022 the Authors

**Rights:** CC BY 4.0

**Rights url:** <https://creativecommons.org/licenses/by/4.0/>

**Please cite the original version:**

Korpelin, V., Melander, M. M., & Honkala, K. (2022). Reducing the Irreducible : Dispersed Metal Atoms Facilitate Reduction of Irreducible Oxides. *Journal of Physical Chemistry C*, 126(2), 933-945. <https://doi.org/10.1021/acs.jpcc.1c08979>

# Reducing the Irreducible: Dispersed Metal Atoms Facilitate Reduction of Irreducible Oxides

Ville Korpelin, Marko M. Melander, and Karoliina Honkala\*



Cite This: <https://doi.org/10.1021/acs.jpcc.1c08979>



Read Online

ACCESS |



Metrics & More

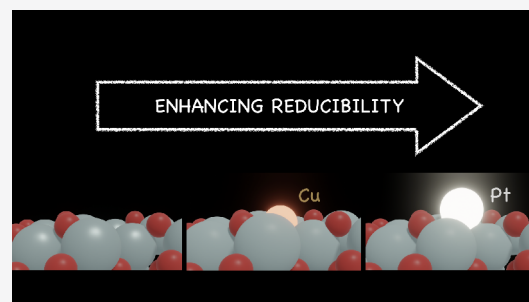


Article Recommendations



Supporting Information

**ABSTRACT:** Oxide reducibility is a central concept quantifying the role of the support in catalysis. While reducible oxides are often considered catalytically active, irreducible oxides are seen as inert supports. Enhancing the reducibility of irreducible oxides has, however, emerged as an effective way to increase their catalytic activity while retaining their inherent thermal stability. In this work, we focus on the prospect of using single metal atoms to increase the reducibility of a prototypical irreducible oxide, zirconia. Based on extensive self-consistent DFT+*U* calculations, we demonstrate that single metal atoms significantly improve and tune the surface reducibility of zirconia. Detailed analysis of the observed single atom induced reducibility allows us to attribute the enhanced reducibility to strong interactions between the metal atom and the electrons trapped in the vacancy and d–p orbital interactions between the metal atom and oxygen. This analysis enables transferring the obtained theoretical understanding to other irreducible oxides as well. The detailed understanding of how oxide reducibility can be tuned offers precise control over the catalytic properties of metal oxides.



## 1. INTRODUCTION

Metal oxides play a crucial role in heterogeneous catalysis, where they are considered as both catalysts and support materials,<sup>1</sup> but this division is artificial, as oxides often play multiple roles.<sup>1</sup> In particular, the catalyst–oxide interfaces may be more active than the catalyst and oxide phases alone<sup>2–5</sup> with some elementary steps taking place on the support oxide and others on the metal catalyst.<sup>6</sup> The oxide may also play an integral role in stabilizing the catalyst and in preventing catalyst sintering.<sup>3,7</sup> Given such diverse roles of metal oxides in catalysis, utilizing, modifying, and understanding their chemistry offers a powerful tool to tailor the performance of heterogeneous catalysts.

Structural defects are known to have a substantial influence on the physical and chemical properties of oxides. In particular, the ability to form oxygen vacancies, that is, the oxide reducibility, is central to the catalytic properties of metal oxides.<sup>6,8</sup> The reducibility determines the oxide's propensity to catalyze, for example, Mars-van Krevelen-type elementary steps, dehydrogenation, and redox reactions.<sup>9</sup> Metal oxides can be roughly divided into reducible and irreducible oxides where the former are characterized by facile oxygen vacancy formation, small band gaps, and the active redox properties of metal cations, which can adopt electrons remaining on the oxide surface.<sup>6,8</sup> Irreducible oxides, on the other hand, have large band gaps, and the electrons cannot localize on the cations, which leads to high vacancy formation energies.<sup>6</sup> From these perspectives, irreducible oxides are often considered as inert supports, while reducible oxides are thought to be more catalytically active.<sup>6,8</sup>

An attractive venue to modify or tailor metal oxide catalysis is to activate surfaces of irreducible oxides while retaining their bulk stability to realize thermally stable oxide supports with enhanced catalytic activity. Thus far, three approaches to enhance the reducibility of irreducible oxides have been identified: nanostructuring, bulk doping, and metal-oxide interfaces.<sup>6</sup> The first two affect both the surface and the bulk properties of the oxide, which may decrease their bulk stability. The last one modifies only the surface properties, which is beneficial in retaining the bulk stability while simultaneously enhancing surface reducibility to activate the oxide toward catalytic applications.

Recently, the above strategies have been successfully applied in the activation of a typical irreducible oxide, zirconia (ZrO<sub>2</sub>), for nonoxidative dehydrogenation of hydrocarbons by creating oxygen vacancies on the surface of monoclinic zirconia.<sup>10</sup> From a mechanistic perspective, the introduction of oxygen vacancies leads to the formation of coordinatively unsaturated Zr cations, which are active sites for the dehydrogenation reaction.<sup>10–12</sup> Crucially, the catalytic activity of ZrO<sub>2</sub> has been directly correlated with its ability to release oxygen, that is, zirconia's reducibility.<sup>10,13</sup> The reducibility and catalytic activity toward

**Received:** October 14, 2021

**Revised:** December 10, 2021

hydrocarbon dehydrogenation have successfully been increased by reducing the  $\text{ZrO}_2$  particle size.<sup>11,12</sup> Doping  $\text{ZrO}_2$  with  $\text{Ca}^{2+}$ ,  $\text{Mg}^{2+}$ , and  $\text{Li}^+$  decreases the activity below that of pristine zirconia, whereas introducing  $\text{La}^{3+}$ ,  $\text{Y}^{3+}$ , and  $\text{Sm}^{3+}$  dopants promotes reducibility and activity.<sup>14,15</sup> Cr-promoted  $\text{ZrO}_2$  was even found to outperform the commercial  $\text{CrO}_x\text{-K/Al}_2\text{O}_3$  catalyst for propane dehydrogenation.<sup>13</sup> In general, tuning the reducibility of zirconia through size-control or doping are envisioned as means to develop eco-friendly and cost-efficient hydrocarbon dehydrogenation catalysts.<sup>13</sup> However, while the oxygen vacancies are crucial for enhancing the activity of  $\text{ZrO}_2$ , it remains poorly understood how and why different dopants or variations in crystal size enhance the reducibility.

In addition to structuring and doping, adsorbed metal clusters have been found to enhance zirconia's reducibility. The effects of an adsorbed  $\text{Ru}_{10}$  cluster<sup>6</sup> and an Au nanorod<sup>16</sup> on the reducibility of  $t\text{-ZrO}_2$  have been computationally investigated, and both were found to significantly stabilize nearby oxygen vacancies. One of the present authors has shown that small Rh clusters and single Rh atoms on zirconia increase the reducibility more than large metal-oxide interfaces.<sup>17</sup> Guided by these results, we now consider a new approach to enhance the surface reducibility of  $\text{ZrO}_2$  with individual dispersed metal atoms. Using single atoms (SA) maximizes metal utilization and greatly facilitates the surface reducibility as shown herein. SAs themselves exhibit catalytic properties distinct from clusters and nanoparticles, but are often unstable and sinter easily.<sup>18</sup> SAs are, however, significantly stabilized when anchored in oxygen vacancies.<sup>7,19</sup> This way the SA-enhanced reducibility can be used for dynamically introducing vacancies to stabilize the SAs for catalytic applications. Besides modifying the reducibility of a specific oxide using SAs, it is crucial to understand to what extent and why certain metal atoms impact oxygen vacancy formation. The atomic level understanding gained for SA-enhanced reducibility on one specific oxide can be transferred to other oxides.

In this work, we have addressed the ability of several different metal SAs to modify the reducibility of zirconia ( $\text{ZrO}_2$ ), a widely utilized and highly irreducible metal oxide support. The (111) facet of monoclinic  $\text{ZrO}_2$  was chosen as the model surface based on its catalytic relevance and high stability, which makes it a robust system for probing reducibility enhancement. Making use of extensive Hubbard-corrected density functional theory (DFT+ $U$ ) calculations we show how different metal SAs affect the reducibility and analyze in detail the reasons behind this behavior. To obtain a reliable DFT description of the electronic structure, we implemented and utilized the self-consistent Hubbard-corrected DFT approach and developed several electronic structure, charge transfer, and covalent bond analyses to explain and understand the SA-induced reducibility. We demonstrate that the detailed understanding obtained for zirconia can be transferred to other irreducible oxides, such as  $\text{MgO}$ , but not to reducible oxides, such as  $\text{TiO}_2$ . In general, the work herein establishes the possibility of rationally enhancing and tuning the reducibility of irreducible oxide surfaces through the use of deposited single metal atoms.

## 2. METHODS

**2.1. DFT Calculations.** Spin-polarized density functional theory (DFT) calculations were performed using GPAW 1.1.0<sup>20–23</sup> together with the Perdew–Burke–Ernzerhof (PBE)

exchange-correlation functional.<sup>24,25</sup> As discussed in section 2.2, a Hubbard+ $U$  correction was also applied on the Zr d electrons. The core electrons of each element were represented by PAW<sup>26</sup> setups in the frozen-core approximation. The reciprocal space of the bulk  $m\text{-ZrO}_2$  unit cell was sampled by a  $(6 \times 6 \times 6)$  Monkhorst–Pack k-point mesh, while for the  $m\text{-ZrO}_2(\bar{1}11)$  surface, modeled with a four-layer thick  $3 \times 3$  cell, only the  $\Gamma$  point was sampled; both choices have been validated in previous studies.<sup>17,27</sup> The slab calculations were performed with periodic boundary conditions in three dimensions with  $\sim 2$  nm vacuum between slabs in the vertical direction. The wave functions and the electron density were described on a real-space grid with maximum spacing  $0.20 \text{ \AA}$ , and atomic structures were allowed to relax until the maximum residual force fell below  $0.05 \text{ eV \AA}^{-1}$ . To validate this choice, selected systems were converged to  $0.025 \text{ eV \AA}^{-1}$ , but the effect on energy and geometry was minor. The lattice parameters and adsorption geometries were reoptimized for each different value of  $U$ .

The reference energies for gas-phase metal atoms were computed in a  $12.00 \text{ \AA} \times 12.01 \text{ \AA} \times 12.02 \text{ \AA}$  cell with the atom shifted  $0.1 \text{ \AA}$  from the center to improve convergence. The magnetic moments were fixed to their known experimental values, and a Fermi–Dirac smearing temperature of  $232 \text{ K}$  was applied. Most atoms converged to their experimental electronic structures, with the exception of Co and Ir, for which we found the configuration  $d^8s^1$  instead of  $d^7s^2$ . For Ni, which is known to have very close-lying  $d^8s^2$  and  $d^9s^1$  configurations,<sup>28</sup> we obtained the latter one. More details are presented in the Supporting Information (SI), section S1. When the metals were adsorbed on the surface, their magnetic moments were allowed to relax freely.

**2.2. Computation of the  $U$  Parameter.** The Hubbard+ $U$  correction to DFT exchange-correlation functionals reduces the electron self-interaction error present in all current DFT functionals.<sup>29</sup> In transition oxide materials, the + $U$  correction accounts for the strong correlation within localized d and f states, reduces the delocalization error of electrons in these states and improves the electronic structure description. Therefore, the Hubbard correction is usually only applied to the metal atoms in transition metal oxides. This approach has been commonly used for  $\text{ZrO}_2$  to improve electron localization while also widening the band gap.<sup>9,16,30,31</sup> We chose to follow this approach as well, but decided to take a closer look at the choice of the  $U$  parameter.

The  $U$  parameter is usually determined semiempirically by varying its value until the obtained result matches some experimental parameter, such as a band gap, as discussed in section S3.1 in the Supporting Information. While this approach can be well-justified, care must be taken, as improving the value of one parameter by changing a  $U$  value might worsen the others.<sup>32</sup> Furthermore, a given  $U$  value is not generally transferable between different DFT implementations, as the value is sensitive to the underlying basis set, pseudopotential, and so on (see SI). To reduce the empiricism and code-dependency of the DFT+ $U$  method, several schemes have been introduced to self-consistently compute the  $U$  parameter (see SI). The benefit of such ab initio methods is that they avoid any parameter transferability issues that might arise between codes or systems and allow direct computation of the  $U$  value for the system of interest.

To reliably estimate the  $U$  values, we implemented the self-consistent linear response method (LR-DFT+ $U$ )<sup>33,34</sup> into the

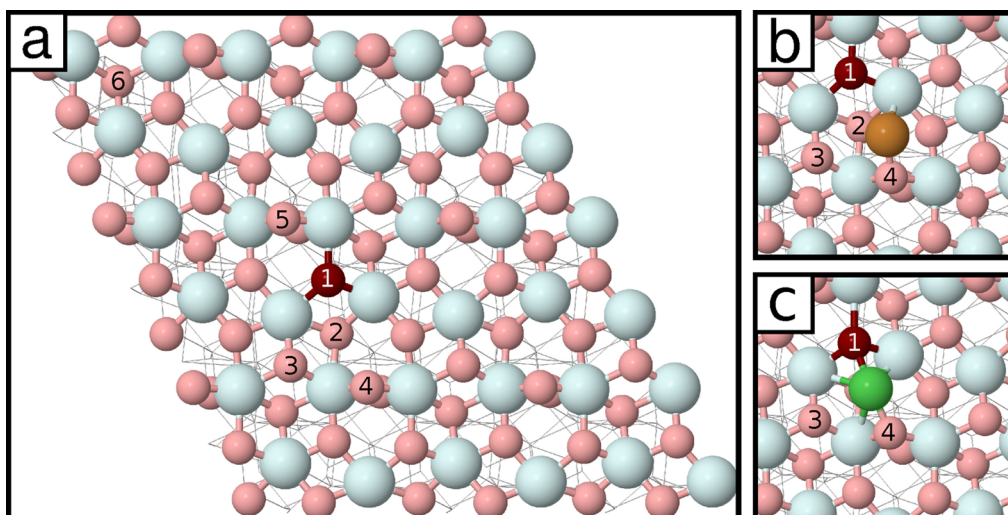


**Figure 1.** (a) Computational  $m\text{-ZrO}_2(\bar{1}11)$  cell. Light blue: Zr, light red: O, dark red: the O atom that is removed to create the vacancy O1. The O atoms important for our discussion have been numbered for clarity. (b, c) Cu (brown) and Ni (green) as representative examples of metal–surface binding geometries.

GPAW software (see SI, section S3 for details) within the simplified, rotationally invariant DFT+ $U$  method by Dudarev et al.<sup>35</sup> This implementation was used to compute the  $U$  value for the Zr d electrons. While an oxygen p correction has been found to improve the description of, for example, bond lengths and electronic structures in some cases,<sup>36–39</sup> no such correction was employed herein.

For bulk  $m\text{-ZrO}_2$ , we computed the Hubbard  $U$  parameter in a  $2 \times 2 \times 2$  supercell (96 atoms). The background correction<sup>33</sup> had only a negligible effect on the result, indicating that the size of the supercell is sufficient. The obtained  $U_d$  value is 1.9 eV, giving the following the cell parameters (without  $U$ ):  $a = 5.197$  (5.161) Å,  $b = 5.263$  (5.231) Å,  $c = 5.365$  (5.340) Å, and  $\beta = 99.6$  (99.6) degrees. The changes are minor and as such it was not considered necessary to do a structurally self-consistent  $U$  determination.<sup>40</sup>

The appropriate  $U$  parameter for a given orbital can depend on its local chemical environment, and therefore, we also calculated the Hubbard  $U$  parameter for the  $m\text{-ZrO}_2(\bar{1}11)$  surface using a four-layer thick  $2 \times 2 \times 1$  supercell (in total 192 atoms). For the top-layer Zr atoms, we obtained  $U_d = 1.9$  eV, while for the second-layer Zr atoms, the corresponding value was 1.8 eV. This demonstrates that the effect of the local environment is minor, as the values are similar to the one computed for the bulk. This small variation was neglected, and we employed  $U_d = 2.0$  eV for all Zr atoms in the slab.

We also considered  $U_d(\text{Zr}) = 4.0$  eV, which is a fairly common choice in the literature,<sup>9,16,30,31</sup> to elucidate the effect of the Hubbard correction on our results. In general, due to the possible transferability issues,  $U$  values taken from the literature should be validated using the specific computational method and system one is studying. In this case, the difference in TM adsorption energies between the  $U = 2.0$  eV and  $U = 4.0$  eV calculations was found to be modest; a detailed comparison is presented in the SI, section S6. The insensitivity of adsorption energy to metal  $U$  in early TM oxides has been noted before in a study highlighting the divergent surface energetics between DFT+ $U$  and hybrid functionals.<sup>41</sup>

As it is well-known that GGA functionals underestimate the band gaps of semiconductors and insulators<sup>42</sup> and the Hubbard correction can, at least partially, correct this, we

examined the impact of the Hubbard  $U$  parameter on the band gaps of the  $m\text{-ZrO}_2$  bulk and surface via a density of states (DOS) analysis. Note that since freezing the bottom two layers of the slab introduces spurious constraint-induced gap states,<sup>43</sup> only the electronic states originating from the unconstrained surface layers are analyzed (see SI, section S2). Comparison with experiment is complicated by the fact that various experimental band gap values for  $m\text{-ZrO}_2$  have been reported in the 4.2–5.8 eV range, depending on the method.<sup>44–47</sup> The reason behind this wide variation between measurements has not been conclusively addressed, though at least the presence of defect states<sup>46</sup> and resolution issues<sup>48</sup> have been suggested as explanations. At any rate, we find that our uncorrected ( $U = 0$ ) bulk band gap value of 3.7 eV lies below the experimental range as expected, and the gap widens with increasing  $U$ , bringing it closer to the measured values. Our LR value  $U_d(\text{Zr}) = 2.0$  eV produces a bulk band gap of 4.1 eV, and increasing the correction to 4.0 eV widens the gap to 4.5 eV. The  $m\text{-ZrO}_2(\bar{1}11)$  surface band gap was computed to be 3.6 eV for both  $U_d(\text{Zr}) = 2.0$  eV and  $U_d(\text{Zr}) = 4.0$  eV. Introducing the oxygen vacancy into the surface leads to the formation of a gap state  $\sim 2.8$  eV above the valence band (VB) edge. Our findings agree with a previous PBE+ $U$  study, which reported a band gap of 3.2 eV and the appearance of a gap state 2.6 eV above the VB.<sup>30</sup>

**2.3. Analyzing Reduction Energies.** The adsorption energy of a transition metal atom M on  $\text{ZrO}_2$  is defined as follows:

$$E_{\text{ads}} = E(\text{M}/\text{ZrO}_2) - E(\text{ZrO}_2) - E(\text{M}, \text{g}) \quad (1)$$

where  $E(\text{M}/\text{ZrO}_2)$  is the total energy of a  $\text{ZrO}_2$  slab with an adsorbed metal atom M,  $E(\text{ZrO}_2)$  stands for the energy of the slab without any adsorbate, and  $E(\text{M}, \text{g})$  corresponds to the energy of a gas-phase metal atom M. Here,  $\text{ZrO}_2$  can be either the ideal or reduced surface.

The reduction energy of a system is computed as

$$E_{\text{R}} = E_{\text{red}} + E(\text{H}_2\text{O}, \text{g}) - E_{\text{stoich}} - E(\text{H}_2, \text{g}) \quad (2)$$

where  $E_{\text{red}}$  and  $E_{\text{stoich}}$  are the respective energies of the reduced and stoichiometric systems, whereas  $E(\text{H}_2\text{O}, \text{g})$  and  $E(\text{H}_2, \text{g})$  are the energies of gas-phase water and molecular hydrogen,

respectively. Water was selected as a reference instead of molecular oxygen, since the energy of O<sub>2</sub> is not accurately described by DFT.<sup>49,50</sup>

We applied several analyses to understand the transition metal (TM) adsorption energies and their effect on the reducibility of *m*-ZrO<sub>2</sub>( $\bar{1}11$ ). The atomic charges were computed using the Bader partition scheme and the algorithm by Henkelman et al.<sup>51</sup>

To quantify orbital hybridization and covalent bonding, we employed a modified version of the hybridization index  $H_{kl}$  proposed in ref 52. The hybridization index is defined as

$$H_{kl}^{IJ} = \sum_{i=1}^{N_e} \sum_{m,m'} w_{km,i}^I w_{lm',i}^J \quad (3)$$

where  $k$  and  $l$  are the angular quantum numbers of interest for atoms  $I$  and  $J$ ,  $m$  and  $m'$  are the corresponding magnetic quantum numbers and  $i$  runs over all  $N_e$  occupied bands. The weight parameter  $w_{km,i}^I = \langle \phi_{km}^I | \psi_i \rangle$  represents the projection of the  $km$  atomic orbital  $\phi$  of atom  $I$  on band  $\psi_i$  obtained from the DFT+ $U$  calculations. The PAW<sup>26</sup> pseudoprojector  $\tilde{p}_{km}^I$  is utilized when approximating the weight as  $w_{km,i}^I \approx \langle \tilde{p}_{km}^I | \psi_i \rangle$ .<sup>21</sup> In practice, summing over all the bands introduces spurious hybridization contributions from bands that are close to each other in energy but spatially distant. To avoid this, we only sum over the bands that have large weight on one of the orbitals of interest, typically  $w > 0.1$  for metal orbitals  $M_d$ . Note that the hybridization index is a qualitative measure, but it can nonetheless be useful for characterizing the metal–surface bonding as we show herein.

### 3. RESULTS AND DISCUSSION

**3.1. Deposition of Single Transition Metal Atoms on ZrO<sub>2</sub>.** The studied *m*-ZrO<sub>2</sub>( $\bar{1}11$ ) surface is rather complex and exhibits a variety of differently coordinated surface anion and cation sites for adsorption, as shown in Figure 1. The majority of the exposed Zr atoms are 6-coordinated, but there are some 7-coordinated cations as in the *m*-ZrO<sub>2</sub> bulk. The surface anions have coordination numbers 2, 3, and 4, and the least endothermic oxygen vacancy formation energy (i.e., reduction energy),  $\sim 3.2$  eV, is obtained for a four-coordinated oxygen atom (O6 in Figure 1a).<sup>17</sup>

We explored the influence of an adsorbed metal atom on the reduction energy by depositing single transition metal (TM) atoms one by one on both ideal and O-deficient *m*-ZrO<sub>2</sub>( $\bar{1}11$ ). Owing to the relatively large computational cell, shown in Figure 1a, the TM atom coverage is low (ca. 1 atom/4 nm<sup>2</sup>) and the TM atoms can be considered nearly isolated. Previously, we have found a Rh atom to favor binding atop the four-coordinated O2 anion (Figure 1a) on the pristine ZrO<sub>2</sub> surface<sup>17</sup> and, therefore, selected the same site for the present systematic screening study. As the focus of this study is in the comparison of the reducibility-enhancing properties of different single metal atoms rather than in identifying the most favorable adsorption site for each metal atom on *m*-ZrO<sub>2</sub>( $\bar{1}11$ ), the other sites are only considered in selected cases. Excluding site variation by focusing on a single adsorption site facilitates the direct comparison of metal properties. With the Rh atom on the O2 site (see Figure 1), the reduction energy was found to vary from one surface anion to the other, highlighting the different coordinations of lattice oxygen anions. The lowest vacancy formation energy, 0.70 eV, was computed for the O1 anion nearest to the O2 anion, with Rh shown in Figure 1a.<sup>17</sup>

Below, the vacancy formation energies, that is, reduction energies, are always computed for the O1 vacancy to ensure comparability between different adsorbed metals.

When an O1 vacancy is formed by removing the corresponding oxygen atom from the pristine *m*-ZrO<sub>2</sub>( $\bar{1}11$ ), two electrons are trapped inside the vacancy, which is usual for irreducible oxides. Bader analysis does not locate a charge maximum at the vacancy site and the surrounding three Zr<sup>4+</sup> cations instead gain 1.17 electrons in total. This observation is in agreement with previous results,<sup>17,30</sup> and the additional charge on the cations is close to the negative Bader charge residing on a surface O<sup>2-</sup> anion. This does not imply that the surface cations are reduced; the resulting state is a singlet, and a PDOS analysis (Figure S4 in the SI, section 7.3) reveals no net magnetic moment on any of the nearby cations. We conclude that the added charge on the cations is simply a feature of the charge partitioning scheme.

To explore the TM-induced reducibility of *m*-ZrO<sub>2</sub>( $\bar{1}11$ ), we consider the following 13 transition metals: Fe, Co, Ni, Cu, Mo, Ru, Rh, Pd, Ag, Re, Ir, Pt, and Au. The set consists of the nine naturally occurring elements from groups 9–11 and four elements (Fe, Mo, Ru, Re) from groups 6–8. These metals were selected based on their importance in catalysis and their different chemical properties to gain a broad understanding of their influence on zirconia reducibility without having to compute through the entire d block.

On the O2 site of the ideal ZrO<sub>2</sub> surface, each metal atom forms a bond with O4, a nearby two-coordinated oxygen anion (bond distances 1.9–2.4 Å). This interaction gives rise to a unique property of the O2 site: the deposited metal atom does not readily accept charge from a distant vacancy, preventing reducibility enhancement when the metal atom does not enter the vacancy. This effect will be discussed in more detail later on in Section 3.3. The copper group metals (Cu, Ag, Au) only bind to the O4 anion, while TMs from other groups interact to some extent also with the other three nearby oxygen anions O1–O3. Comparison of the computed M–O bond lengths indicates that Pd, Ir, and Pt bind to two out of the four available O anions, while the rest bind to three of them. Here we consider two atoms bound if their distance is less than the sum of the covalent radius of the TM atom<sup>53</sup> and the radius of the oxide anion<sup>54</sup> (1.26 Å). The varying adsorption behavior arises from the relatively diverse surface structure and atom coordination of *m*-ZrO<sub>2</sub>( $\bar{1}11$ ), as described earlier. The exact metal–oxide distances are provided in Table S3.

On the defected surface created by removing O1, most metal atoms migrated to this vacancy during structure optimization, while the group 6–8 metals Fe, Mo, Ru, and Re remained in the original O2 site. Manually placing these atoms into the O1 vacancy enhances the adsorption energies by up to 2.0 eV, which means that adsorption in the vacancy site is also thermodynamically more favorable for these atoms as well. The structural characteristics of the adsorbed metals inside the vacancy exhibit some clear differences: while the copper and nickel group metals and Co remain essentially in the center of the vacancy with their distances to the surrounding Zr atoms being 2.6–3.1 Å, the others migrate toward a nearby Zr bridge site due to interaction with the two-coordinated O5. This phenomenon is particularly notable for the group 6–8 metals forming a bond with the O5 atom (bond distance ca. 2 Å).

**3.2. Adsorption and Reduction Energies.** In this subsection, we address the thermodynamics of TM adsorption

on the pristine  $m\text{-ZrO}_2(\bar{1}11)$  and inside the O1 vacancy. This is followed by a comparison with the literature on MgO and  $\text{TiO}_2$  and a discussion on the reduction energies of  $m\text{-ZrO}_2(\bar{1}11)$ . Finally, the feasibility of further reduction and the distance dependence of the reducibility enhancement are briefly considered.

The TM adsorption energies on the pristine surface range from  $-2.89$  to  $-0.60$  eV (see Table 1) and mostly follow a

**Table 1. Adsorption ( $E_{\text{ads}}$ ) and Reduction ( $E_{\text{R}}$ ) Energies (eV), Bader Charges, and Atomic Spin Moments for Each Adsorbed Metal Atom<sup>a</sup>**

| metal | on pristine                 |        |      | in vacancy                  |        |      | $E_{\text{R}}$ |
|-------|-----------------------------|--------|------|-----------------------------|--------|------|----------------|
|       | $E_{\text{ads}}^{\text{p}}$ | charge | spin | $E_{\text{ads}}^{\text{d}}$ | charge | spin |                |
| Fe    | -1.50                       | +0.34  | 3.78 | -3.53                       | -0.38  | 2.48 | 1.79           |
| Co    | -1.90                       | +0.35  | 1.17 | -3.53                       | -0.73  | 0.13 | 2.19           |
| Ni    | -2.20                       | +0.21  | 0.00 | -4.73                       | -0.81  | 0.00 | 1.29           |
| Cu    | -1.26                       | +0.07  | 0.56 | -3.08                       | -0.66  | 0.00 | 2.00           |
| Mo    | -1.05                       | +0.48  | 3.72 | -3.00                       | -0.31  | 2.05 | 1.87           |
| Ru    | -2.25                       | +0.22  | 1.92 | -4.95                       | -0.70  | 0.00 | 1.12           |
| Rh    | -2.41                       | +0.10  | 0.91 | -5.43                       | -0.85  | 0.82 | 0.80           |
| Pd    | -1.86                       | +0.02  | 0.00 | -5.00                       | -0.95  | 0.00 | 0.68           |
| Ag    | -0.60                       | +0.03  | 0.52 | -2.61                       | -0.67  | 0.07 | 1.81           |
| Re    | -1.75                       | +0.35  | 2.85 | -4.26                       | -0.57  | 1.05 | 1.31           |
| Ir    | -2.89                       | -0.01  | 0.90 | -6.65                       | -0.95  | 0.86 | 0.06           |
| Pt    | -2.82                       | -0.09  | 0.00 | -7.25                       | -1.05  | 0.00 | -0.61          |
| Au    | -0.92                       | -0.13  | 0.58 | -3.92                       | -0.82  | 0.00 | 0.82           |

<sup>a</sup> $E_{\text{R}}$  for the O1 vacancy on the ideal surface without an adsorbed metal atom is 3.82 eV.

clear periodic trend:  $E_{\text{ads}}$  becomes more exothermic when moving from left to right and from top to bottom in the periodic table. The Cu group metals are an exception, as their adsorption is fairly weak ( $-1.26$  to  $-0.60$  eV) even though in the periodic table they are located to the right of all other studied TMs. Pd also binds weaker than Ni and Rh, the elements directly above and to the left of it. We propose that the closed d shell electronic structure of the Cu group metals and Pd is behind the divergent behavior of these elements, which is also observed in other analyses and discussed in detail in Sections 3.3.1 and 3.3.2.

The results in Table 1 show that TM adsorption in the O1 vacancy is significantly more exothermic than on the pristine surface. The in-vacancy adsorption energies also present a wider range of values, varying from  $-7.25$  eV for Pt to  $-2.61$  eV for Ag. The vacancy adsorption energies follow the same trend that was observed for the ideal surface. In general, the adsorption energy of a TM atom in the O1 vacancy is at least 1.6 eV more exothermic than on the O2 site of the defect-free surface. Particularly exothermic vacancy adsorption energies are found for Ir ( $-6.65$  eV) and Pt ( $-7.25$  eV). Figure 2 displays that the adsorption energies on the pristine surface ( $E_{\text{ads}}^{\text{p}}$ ) and inside the vacancy ( $E_{\text{ads}}^{\text{d}}$ ) are strongly linked to each other, which we briefly discuss later in Section 3.3.2.

Next, we compare our results with previous studies on irreducible (MgO,<sup>55–59</sup>  $\text{ZrO}_2$ <sup>60</sup>) and reducible ( $\text{TiO}_2$ <sup>61,62</sup>) oxides. Computational studies of single TM atom adsorption on  $\text{ZrO}_2$  at the DFT-GGA level of theory have focused on Pt, Pd, and Rh<sup>60</sup> and the Cu group on the ideal  $c\text{-ZrO}_2(111)$  surface.<sup>63</sup> In line with our findings, these results for  $\text{ZrO}_2$  highlight that Pd adsorbs less strongly than Rh and Pt,<sup>60</sup> while the comparison between Rh and Pt adsorption energies is less

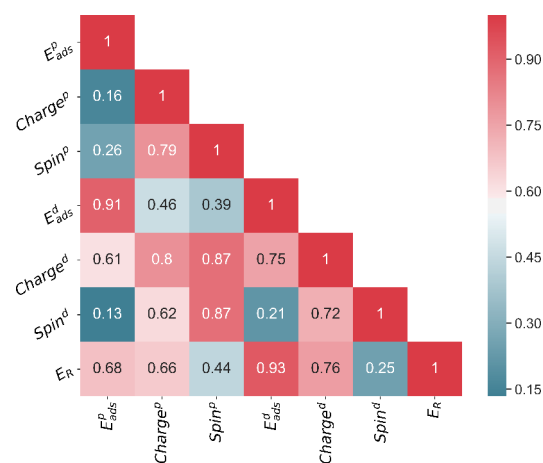


**Figure 2.** Pearson correlations between the values presented in Table 1. “p” and “d” stand for pristine and defected, respectively.

clear due to the strong site-dependency. Our adsorption energy trend also agrees with that observed for the Cu group ( $\text{Cu} < \text{Au} < \text{Ag}$ ) on the cubic surface.<sup>63</sup>

MgO is an irreducible oxide like  $\text{ZrO}_2$ , though it is more ionic in character and has an even higher vacancy formation energy.<sup>64</sup> In terms of the surface structure,  $\text{MgO}(001)$  is highly symmetric: all top-layer Mg and O atoms are equivalent to each other.  $m\text{-ZrO}_2(\bar{1}11)$ , on the other hand, is a relatively complex surface, as discussed earlier. The adsorption behavior on both ideal and defected  $m\text{-ZrO}_2(\bar{1}11)$  is broadly similar to what has been reported for the corresponding  $\text{MgO}(001)$  surfaces. On both surfaces, the adsorption energies exhibit similar trends, and the predicted spin states of the metals largely agree.<sup>58,59</sup> This is in accordance with the qualitatively similar properties of the oxides, and also their defects; on both MgO and  $\text{ZrO}_2$ , the vacancy electrons are trapped inside the vacancy, as they are not able to reduce the surface cations. Thus, the trends observed in the present work can likely be generalized for other irreducible oxides as well. There are some exceptions to the trends between MgO and  $\text{ZrO}_2$ , but they can be rationalized based on the differing geometries of the two oxide surfaces. A more comprehensive comparison is presented in the SI, section S4.

In contrast to MgO and  $\text{ZrO}_2$ ,  $\text{TiO}_2$  is reducible. The adsorption of the first TM row metals, as well as Pd, Ir, Pt and Au, has been studied using GGA-DFT on both pristine and defected rutile  $\text{TiO}_2(110)$  surfaces.<sup>61,62</sup> Contrary to the results obtained for  $\text{ZrO}_2$  and MgO, the adsorption energies of the studied metal atoms in the  $\text{TiO}_2$  vacancy are typically more endothermic than or roughly equal to the corresponding energies on the ideal surface.<sup>62</sup> Only Au and, when the Hubbard correction was introduced, Pt bound more strongly inside a surface vacancy than on the ideal surface, though Pd and Ir were also noted as borderline cases. This comparatively weaker metal–vacancy interaction in reducible oxides is caused by the ability of the vacancy electrons to reduce the oxide cations instead of staying in the vacancy to interact with the adsorbed TM atom. These results suggest that the metal-induced reducibility enhancement is weaker on reducible oxides, and only some TM atoms are able to overcome the tendency of the vacancy electrons to localize on the oxide cations.

After TM adsorption on the pristine surface and in the O1 vacancy, we focus on the enhanced reducibility induced by the

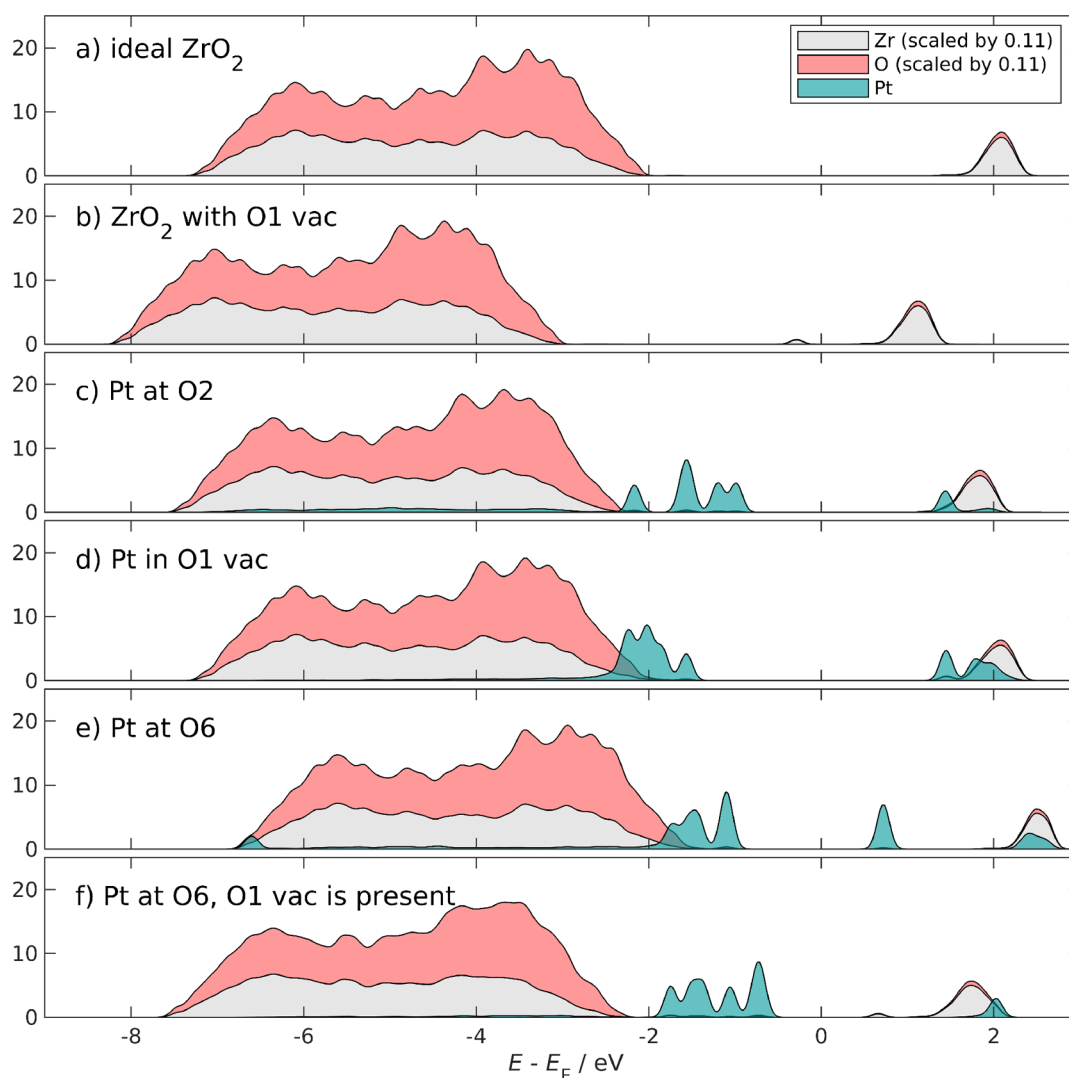


**Figure 3.** Atom-projected densities of states of  $\text{ZrO}_2$  and  $\text{Pt/ZrO}_2$  in various cases. The calculations were spin-polarized, but in these cases, the plots are visually identical for both spin directions and only one is shown. Only the states from the top two layers of the slab are pictured here, since the bottom layers have spurious constraint-induced gap states (see SI, section S2 for details). The DOS's of Zr and O have been scaled by 1/9 for visual clarity; 1/9 of the top two layers corresponds to one unit cell of monoclinic  $\text{ZrO}_2$ .

TM adsorption. The reduction energies computed according to eq 2 using the adsorption energies discussed above are reported in Table 1. In some cases the metal atom resides in the vacancy, whereas as in other cases it is initially more distant from the vacancy, as discussed earlier in Section 3.1. As the adsorption energies on the pristine and defected surfaces correlate strongly with each other (Figure 2), and because the reduction energies are computed as their differences (plus a constant), the trends of  $E_R$  follow those of the adsorption energies discussed above.

The reduction energy of the ideal  $m\text{-ZrO}_2(\bar{1}11)$  surface without any adsorbed TMs is found to be 3.82 eV when the O1 vacancy is formed. Table 1 shows that all of the considered metals lower  $E_R$  considerably. Even though Co causes the weakest effect,  $E_R$  is still lowered by 1.6 eV. On the other hand, the strongest reducibility-enhancing effect is observed for Pt, which actually makes  $E_R$  exothermic, a very unusual observation for an irreducible oxide. It also provides a strong enhancement, with an  $E_R$  of 0.06 eV.

To investigate whether an adsorbed TM atom can enhance a second reduction of the surface, we placed a Pt atom on O6

and formed the O1 and O1' vacancies. Pt was chosen for this test, since it produced the most favorable first reduction. However, we find that the adsorbed Pt atom has essentially no effect on the second reduction energy. Thus, one Pt atom can only facilitate the removal of one oxygen atom as Pt's initially empty electronic states become populated upon vacancy formation. Motivated by an earlier investigation, where the adsorption of Rh on  $m\text{-ZrO}_2(\bar{1}11)$  was suggested to induce an "enhanced reducibility zone" of about 4 Å around the adsorbed Rh atom,<sup>17</sup> we also addressed the spatial effect of the TM-induced reducibility. In this work, we find three distinct classes of reducibility-altering effects depending on the adsorption site of the metal atom. The enhancement is strongest when the adsorbed metal atom is near the removed oxygen atom and fills the vacancy. A weaker, essentially distance-independent (within our computational cell) enhancement is observed for most adsorption sites when the metal stays out of the vacancy. Finally, on a distant O2 site, the adsorbed TM does not enhance the reducibility at all.

**3.3. Analyzing the Adsorption.** Upon the adsorption of a metal atom onto oxide surfaces, multiple interdependent

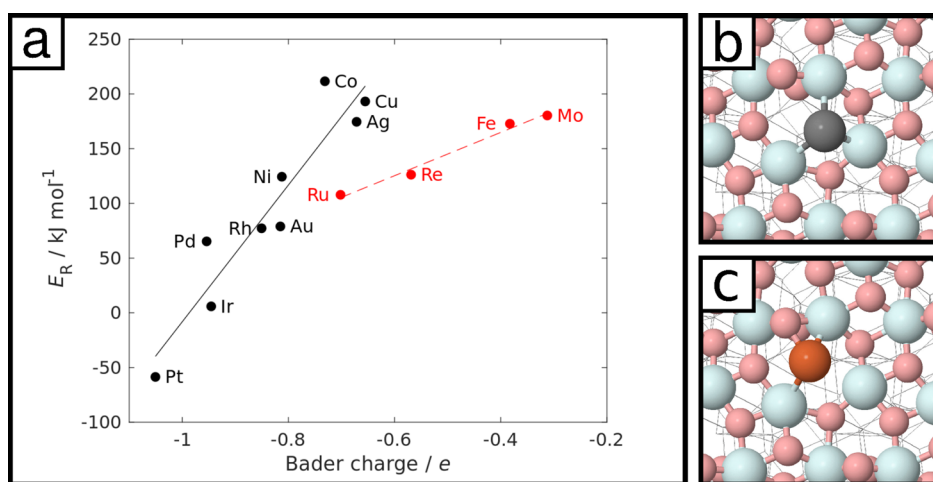


**Figure 4.** (a) The correlation of the reduction energy and the Bader charge of the metal in the vacancy. Solid line ( $R^2 = 0.89$ ): metals that stay in the center of the vacancy. Dashed red line ( $R^2 = 0.98$ ): metals that bond strongly to a nearby two-coordinated O atom. (b) Pt vacancy binding geometry as a representative example of the metals that stay in the center of the vacancy. (c) Fe vacancy binding geometry as a representative example of the metals that bind to the two-coordinated O atom.

phenomena can take place, including charge transfer, metal–surface hybridization, and polarization. In order to understand how these different factors contribute to the TM adsorption and TM-induced reducibility discussed above, we carried out an extensive analysis of the electronic structure, charge transfer, magnetism, energy partitioning, and hybridization. To this end, we have analyzed the density of states (DOS) plots, Bader charges, and magnetic moments of the  $M/\text{ZrO}_2$  systems. We also note that various electronic and thermodynamic properties are strongly correlated, as shown in Figure 2.

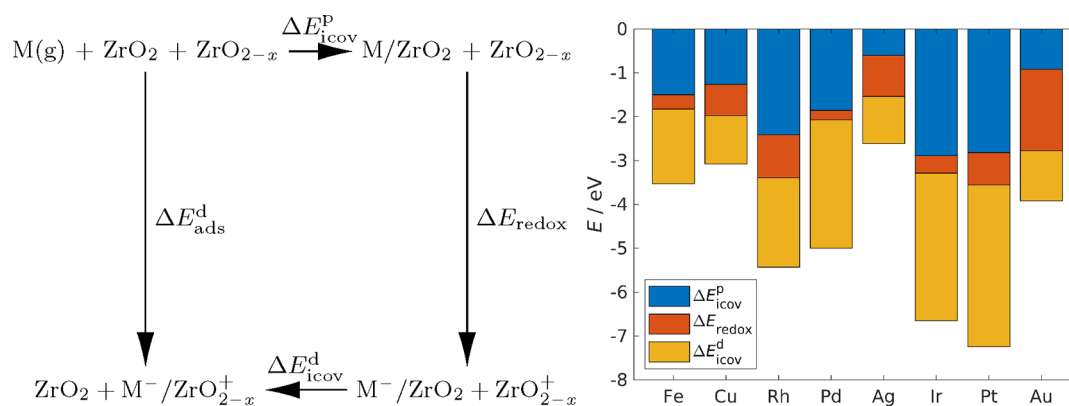
**3.3.1. Electronic Properties of Adsorbed TM Atoms.** The electronic effects are analyzed in terms of the density of states (DOS). Here we focus on platinum, which exhibits the strongest impact on the reducibility, while DOSs for the other elements are shown in SI, section S7. Figure 3 displays the DOS plots for various bare and Pt-adsorbed  $\text{ZrO}_2$  surfaces as examples of typical  $M/\text{ZrO}_2$  electronic structures (see SI, section S5 for  $U = 0$  comparison). As Figure 3a shows, the VB edge of bare  $\text{ZrO}_2$  mainly consists of O 2p states, while the conduction band (CB) is dominated by Zr states. In the presence of an O1 vacancy, a gap state appears just below the Fermi level, see Figure 3b). The majority of the Pt states are located in the band gap near the VB edge, while some states overlap with the CB. Comparison of Figure 3c and d, corresponding to the ideal and defected Pt/ $\text{ZrO}_2$  surfaces, shows that when Pt is in the vacancy its electronic states cluster together and overlap more with the oxide states than on the ideal surface. This suggests that the Pt orbitals hybridize with each other when Pt binds inside the vacancy. This kind of hybridization turns out to be important for vacancy adsorption and will be discussed in detail in Section 3.3.2.

Figure 3c,e demonstrate the difference between the “charge-rejecting” adsorption site, O2, and the “charge-accepting” adsorption site, O6, respectively. A Pt atom at site O6, even when further away from the vacancy, can accept  $\sim 1$  electron from the vacancy and enhance the reducibility of  $\text{ZrO}_2$  by 1.1 eV, whereas Pt at an O2 site far away from the vacancy gains no charge and has no effect on the reducibility. In the case of the O2 site, the DOS analysis (panel c) shows that most available Pt states are already filled, likely due to the Pt–O4 interaction, whereas in the case of the O6 site (panel e), there

are unoccupied Pt states. These can accept electrons from the vacancy, stabilize the vacancy formation, and lead to a more exothermic reduction energy. The unoccupied states become populated even when the vacancy is formed further away, as shown in Figure 3f. The population of these originally unpopulated Pt states leads to a formation of a small peak above the Fermi level (panel f) that is due to the depopulation of the vacancy state, which is occupied when no Pt is present on the surface (Figure 3b). Note that this charge-transfer interaction is mediated by the zirconia atoms, as no direct orbital interaction between the Pt atom and the vacancy is visible in Figure 3f.

To further investigate the charge transfer between the oxide (or vacancy) and the adsorbed TM atom, the Bader charges of the metal atoms were computed and collected into Table 1). Metal atoms are, in general, neutral or slightly positive on the ideal surface, and the largest positive charges were found for the group 6–8 metals for which we obtained values from +0.22 to +0.48 $e$ . Similar values were calculated also for Co and Ni. Ir, Pt, and Au have slightly negative Bader charges, which, however, are small and do not necessarily indicate reduction of the metals. The Bader charges broadly follow the trends in atomic electronegativities and electron affinities, which are presented in detail in the SI (Figure S5). Care should be taken when interpreting computed Bader charges, because the analysis does not solely describe charge transfer and, for example, polarization effects may also have a contribution for an adsorbed metal atom.<sup>65</sup>

The Bader charges of vacancy-bound metal atoms range from  $-1.05$  to  $-0.31e$  and the observed trends are largely similar to those on the nondefected surface, with a strong correlation (0.91, Figure 2) between the in-vacancy and on-surface atoms. A similar correlation is also visible for the adsorption energies on the pristine surface and in the O1 vacancy, which further reinforces the conclusion that the two types of adsorption configurations share similar properties. Based on the Bader analysis, the studied TMs can be grouped into two main categories: Fe, Mo, and the Cu group metals are  $\sim 0.7e$  more negatively charged in the vacancy, while for the other metals, the corresponding value is  $\sim 1.0e$ . This categorization is also reflected in the thermodynamic proper-



**Figure 5.** Left: The thermodynamic cycle used to divide the vacancy adsorption energy into components, following the idea in ref 68. Here,  $M(g)$  is the gas-phase metal atom,  $ZrO_2$  is the bare ideal surface,  $ZrO_{2-x}$  is the bare surface with the O1 vacancy,  $M/ZrO_2$  is the ideal surface with M on site O2,  $M^-/ZrO_2$  is the ideal surface with M on site O6 and 1 e of negative charge,  $ZrO_{2-x}^+$  is  $ZrO_{2-x}$  with 1 e of positive charge, and  $M^-/ZrO_2^+$  is the (noncharged) surface with M in the O1 vacancy. Right: The contributions of each component to the total vacancy adsorption energies. The total length of the bar corresponds to  $\Delta E_{\text{ads}}^{\text{d}}$ . The values have been tabulated in section S11 of the Supporting Information.

ties as atoms in the first category bind weaker than atoms in the second category both on the pristine surface and inside the vacancy. The sole exception is Co binding more weakly than Au in the vacancy, which may be related to the large changes in Co's electronic structure when moving from the pristine surface to vacancy (SI, section S7) and the known difficulties in describing the spin state of Co with DFT.<sup>66,67</sup>

The TM charges correlate strongly also with the reduction energies as shown by Figure 4 for the  $E_{\text{R}}$  and the Bader charge of the vacancy-adsorbed metal atom. While the majority of the studied elements fall on the same line in Figure 4, Fe, Mo, and Re and Ru deviate from the general trend as they bind to the O5 oxygen and reside asymmetrically in the vacancy. We note that a similar correlation between  $E_{\text{R}}$  and the Bader charge is also seen in Figure 2.

To characterize the electronic properties of the adsorbed metal atoms, we computed their magnetic moments upon surface deposition. On ideal  $ZrO_2$ , the gas-phase moments are retained for Fe and the  $d^{10}$  metals, whereas for the other metals, the magnetic moments are quenched by  $2 \mu_{\text{B}}$ . This could be due to surface-induced d-level splitting favoring lower-spin configurations or by hybridization between the metal s and d states and oxygen p states. The vacancy enhances the quenching effect since the vacancy and metal atom orbitals may be mixing with each other. The effect is largest for Mo, Ru and Re, whose magnetic moments are quenched by  $4 \mu_{\text{B}}$  compared to their gas-phase values.

Comparison of the magnetic moments on the ideal surface versus those in the vacancy reveals a periodic trend. The group 6–8 metals (Fe, Mo, Ru, Re) undergo a quenching of  $2 \mu_{\text{B}}$  and bind closely ( $\sim 2.0 \text{ \AA}$ ) to the O5 atom. Of the group 9 metals, Rh and Ir retain their doublet configurations and bind somewhat closely ( $\sim 2.4 \text{ \AA}$ ) to O5, while Co has its moment quenched by  $1 \mu_{\text{B}}$  and remains at the center of the vacancy. Again, the divergent behavior of Co may originate from the intricacies of its spin state description. The group 10 metals (Ni, Pd, Pt) adsorb in the center of the vacancy and are already singlets on the ideal surface, preventing further magnetic quenching. Finally, of the group 11 metals, all of which also adsorb in the center of the vacancy, Cu and Au undergo a quenching by  $1 \mu_{\text{B}}$ , while Ag remains as a doublet even in the vacancy. This is likely explained by its high s–d excitation

energy, which inhibits s–d hybridization, as discussed later in more detail.

**3.3.2. Metal–Vacancy Interaction: Thermodynamic Cycle.** For further analysis of metal–vacancy interaction, we devised the thermodynamic cycle shown in Figure 5. Similar approaches have been previously employed to understand the factors governing Au binding on a doped CaO surface,<sup>68</sup> the adsorption of catalytic intermediates on metal–oxide interfaces,<sup>69</sup> and terephthalic acid monolayer self-assembly.<sup>70</sup> In the cycle, the metal–vacancy interaction is broken down into three components: ionic-covalent on the ideal surface, redox, and ionic-covalent inside the vacancy.

The  $E_{\text{redox}}$  and  $E_{\text{icov}}^{\text{d}}$  components are computed using charged slab calculations in three-dimensional periodic boundary conditions, utilizing a homogeneous compensating background charge to neutralize the cell. To correct for the inconsistency in average electrostatic potential between calculations of different charge states, we have applied a Lany–Zunger-type potential alignment correction (see section S11 in the Supporting Information).<sup>71</sup> The planarly averaged electrostatic potentials were aligned at the midpoint of the frozen part of the slab, resulting in energy corrections of  $-0.21 \text{ eV}$  for the positively charged vacancy and  $-0.18 \text{ eV}$  for the negatively charged metal systems. The identity of the metal was found to have a negligible effect on the electrostatic potential profile, and thus on the alignment correction. In total, this correction results in a  $-0.39 \text{ eV}$  uniform shift to the  $E_{\text{redox}}$  components (and a corresponding  $+0.39 \text{ eV}$  shift to  $E_{\text{icov}}^{\text{d}}$ ). The image charge interaction in charged slab calculations is challenging to treat correctly, and we neglect it here; however, it is not expected to depend strongly on the identity of the metal, so the observed  $E_{\text{redox}}$  trends should be unaffected.

**$\Delta E_{\text{icov}}^{\text{p}}$  Component.** The first component,  $\Delta E_{\text{icov}}^{\text{p}}$ , corresponds to the direct interaction between an adsorbing metal atom and the surface ions. It quantifies the hybridization of metal states with nearby surface orbitals and some charge transfer. The energy change related to this process varies from one metal to another between  $-0.6$  and  $-2.9 \text{ eV}$ , as shown in Figure 5.

The ionic and covalent contributions to  $\Delta E_{\text{icov}}^{\text{p}}$  were studied by correlating the TM Bader charges on the ideal surface against  $\Delta E_{\text{icov}}^{\text{p}}$  and  $\Delta E_{\text{ads}}^{\text{d}}$ . Note that a positive Bader charge does not indicate a reduction of the (irreducible) zirconia, but

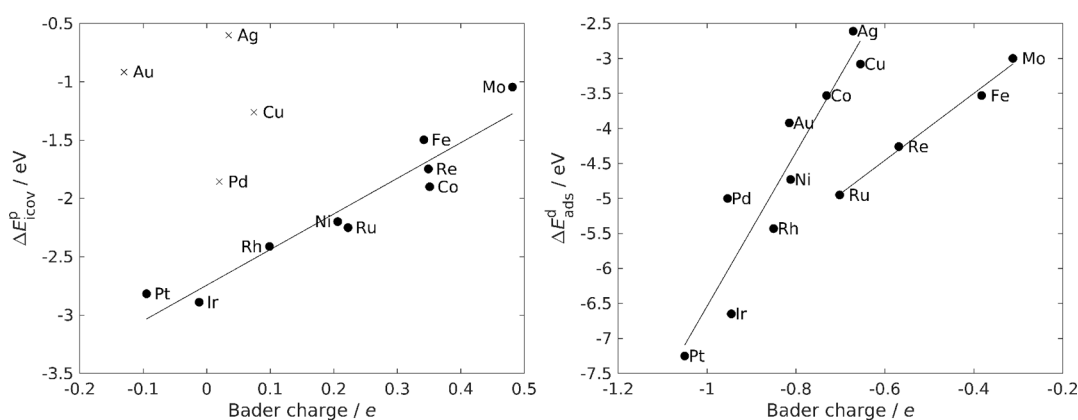


**Figure 6.** Left: the correlation of  $\Delta E_{\text{fcov}}^{\text{p}}$  and the Bader charge of the metal,  $R^2 = 0.91$ . The  $d^{10}$  metals (marked with crosses) have been excluded from the fit. Right: the correlation of  $\Delta E_{\text{ads}}^{\text{d}}$  and the Bader charge of the metal,  $R^2 = 0.87$  (Fe, Mo, Re, Ru excluded) and  $R^2 = 0.99$  (the Fe, Mo, Re, Ru line).

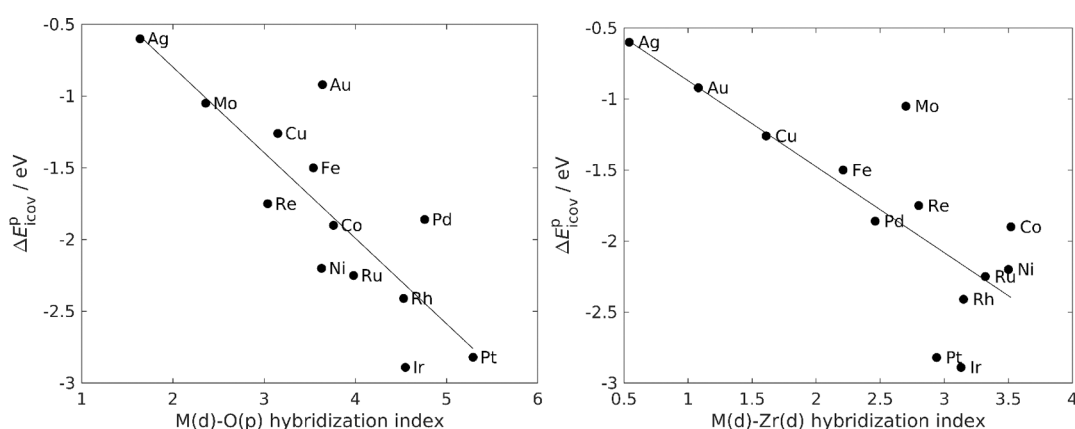


**Figure 7.** Correlations of  $\Delta E_{\text{fcov}}^{\text{p}}$  with  $H_{\text{M(d)}, \text{O(p)}}$  ( $R^2 = 0.69$ ) and  $H_{\text{M(d)}, \text{Zr(d)}}$  ( $R^2 = 0.63$ ). The hybridization indices have been summed over the nearest four atoms of each type.

the variation in Bader charges is considered to arise from the sharing of electrons along metal–surface bonds of partly covalent character. Figure 6 shows that a good correlation between  $\Delta E_{\text{fcov}}^{\text{p}}$  and the Bader charge is found when the  $d^{10}$  metals Cu, Ag, Au, and Pd are excluded. This exclusion is also chemically motivated as these TM atom have a filled d-shell, which cannot accept electrons.

The deviation observed for the  $d^{10}$  metals on the ideal surface suggests that they exhibit qualitatively different adsorption behavior from the others. We note that the deviation is largest for the Cu group  $d^{10}s^1$  metals and somewhat smaller for Pd, which has a  $d^{10}$  structure and lacks a valence  $s$  electron. In studies on MgO(001), the comparatively weak binding of Cu group metals has been ascribed to Pauli repulsion brought on by the mandatory half-occupation of the valence  $s$  state.<sup>56,72</sup> While, for example, Pt also has a half-occupied vacancy  $s$  orbital in the gas phase ( $d^9s^1$ ), it can (and does) reach a stable closed-shell structure upon adsorption due to the available space on the nonfilled  $d$  orbital. This is not possible for the  $d^{10}s^1$  metals in the Cu group.

Good correlations are also found between  $\Delta E_{\text{ads}}^{\text{d}}$  and the Bader charges of the vacancy-bound metal atoms (Figure 6). Here, as with  $E_{\text{R}}$ , the correlation is computed separately for Fe, Mo, Re, and Ru. These four atoms bind in a qualitatively different geometry than the others, as discussed earlier in Section 3.3.1. Notably, unlike with  $\Delta E_{\text{fcov}}^{\text{p}}$  on the ideal surface,

the  $d^{10}$  metals follow the main correlation. This indicates that the  $d^{10}$  metals hybridize in the vacancy and can accept some electrons into these hybrid orbitals.

This deviation of the  $d^{10}$  metals was also investigated by considering the degree of hybridization between the metal and surface orbitals, which measures the covalent character of the metal–surface bonding. Our method of choice is the hybridization index  $H_{kl}$  (eq 3), which provides a measure of the overlap between atomic orbitals in DFT bands, and has been successfully applied for transition metal clusters.<sup>52,73</sup> This index was computed between the metal  $d$  orbitals and surface  $O_{\text{p}}$  and  $Zr_{\text{d}}$  orbitals. To describe the total effect from metal–surface hybridization on the ideal surface, the index is summed over the four oxide (or zirconium) ions nearest to the binding site.

The metal–oxygen hybridization index,  $M_{\text{d}}-O_{\text{p}}$ , correlates rather strongly with  $\Delta E_{\text{fcov}}^{\text{p}}$  ( $R^2 = 0.69$ ), as shown in Figure 7. This implies that metal–oxygen covalent bonding has an important role in determining the  $M$ – $ZrO_2$  binding strength, which agrees with prior work on the subject.<sup>60,63</sup> We stress again that the  $m$ - $ZrO_2$ ( $\bar{1}11$ ) surface allows multiple different metal–oxygen bonds to form, as opposed to simpler surfaces such as MgO(001), where each metal preferentially binds on top of a single O anion. In light of this, the observed correlation is remarkably good.

The  $d^{10}$  deviation discussed above can also be rationalized to some extent with the  $M_{\text{d}}-Zr_{\text{d}}$  hybridization index. The results

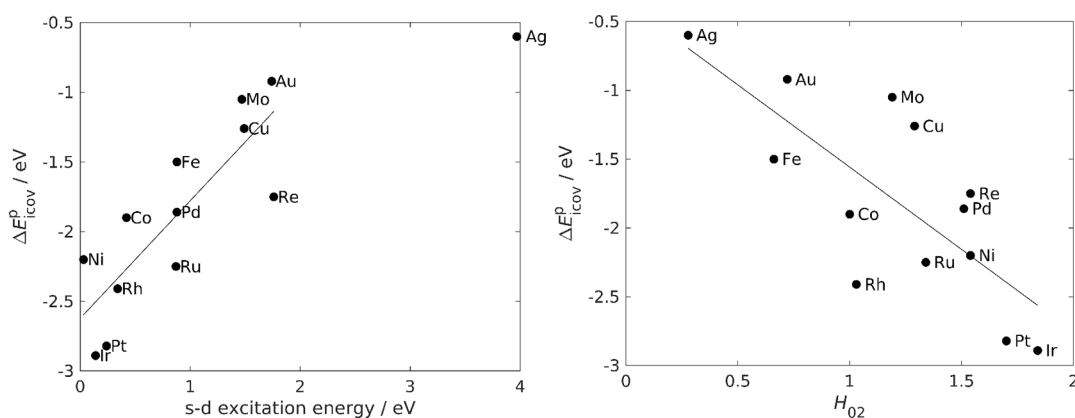


**Figure 8.** Left:  $\Delta E_{icov}^P$  plotted against the s–d excitation energy of the metal from ref 74.  $R^2 = 0.69$  (Ag excluded from fit). Right:  $\Delta E_{icov}^P$  vs  $H_{O2}$ ,  $R^2 = 0.57$ .

in Figure 7 show that the  $d^{10}s^1$  metals are weakly hybridized with Zr, indicating that the d–d interaction is less favorable for them. This is also supported by the adsorption heights of the metals, as the Cu group metals adsorb 0.2–0.5 Å further from the surface plane than the next-highest-adsorbing metal atom (Pd). In fact, the adsorption height correlates well ( $R^2 = 0.91$ ) with the  $M_d$ –Zr<sub>d</sub> hybridization index, while the correlation with the  $M_d$ –O<sub>p</sub> hybridization index is nonexistent ( $R^2 = 0.24$ ). The correlation plots are shown in Figure S6.

We also considered the s–d hybridization in the adsorbed TMs, as this has been previously noted as a contributor to the adsorption strength.<sup>55,63,72</sup> To assess the degree of s–d hybridization, we used two measures. The gas-phase s–d excitation energy corresponds with the energy difference between the s and d levels and thus is expected to correlate with the propensity for s–d hybridization. In addition, using the  $H_{kl}$  index with  $k = 0$  and  $l = 2$ , we can directly estimate the degree of s–d hybridization in our computational system. The index also accounts for the adsorption-induced changes in the electronic structure of the metal atom, while the gas-phase s–d excitation energy lacks this effect.

Both measures were correlated against  $\Delta E_{icov}^P$ . The gas-phase s–d excitation energy produces a reasonable correlation when the Ag outlier is excluded (Figure 8, left). The exclusion of Ag is justified by its very large s–d excitation energy, as even a somewhat smaller value could already preclude any possibility of s–d hybridization. The correlation between  $\Delta E_{icov}^P$  and  $H_{O2}$  turns out to be slightly weaker than the one obtained with the s–d excitation energy, though the extremes still match expectations: Ag has a low degree of hybridization, while Pt and Ir have a high one (Figure 8, right). The decent correlation between  $\Delta E_{icov}^P$  and the gas-phase s–d excitation energy indicates that the surface adsorption does not dramatically alter the relative energies of the s and d orbitals, while the comparatively poorer correlation obtained with  $H_{O2}$  reflects the qualitative nature of the hybridization index.

**$\Delta E_{redox}$  Component.** The  $\Delta E_{redox}$  component describes the redox process where the initial state involves metal atom adsorption on the pristine surface far away from the vacancy. The final state is obtained by adding an electron to M/ZrO<sub>2</sub> and removing it from the ZrO<sub>2-x</sub> system. Note that in the final state, a metal atom is placed on the O6 site, as it is unable to accept charge in the O2 position, as discussed earlier. This choice was justified by verifying that the adsorption energies of Au and Pt atoms on both sites are similar (within 0.25 eV). In

the charged system, the TM atom gains 0.1–1.0e of Bader charge, depending on the metal, and sometimes shifts slightly from the position on the corresponding neutral system. In general, the redox contribution has a small negative value of 0 to –1 eV, except for Au which presents a more substantial redox energy of –1.86 eV. For Ag, the redox component also makes up a considerable part of the vacancy adsorption energy. For the other metals, the low values indicate that charge transfer is not a dominant contributor to the adsorption energy even in the case of vacancy adsorption, and the stabilization instead occurs primarily via metal–vacancy orbital hybridization.

We expect the redox component to depend on the electron affinity of the metal atom, as this contribution highlights the metal’s ability to accept charge. Figure 9 shows that Pd, Rh,

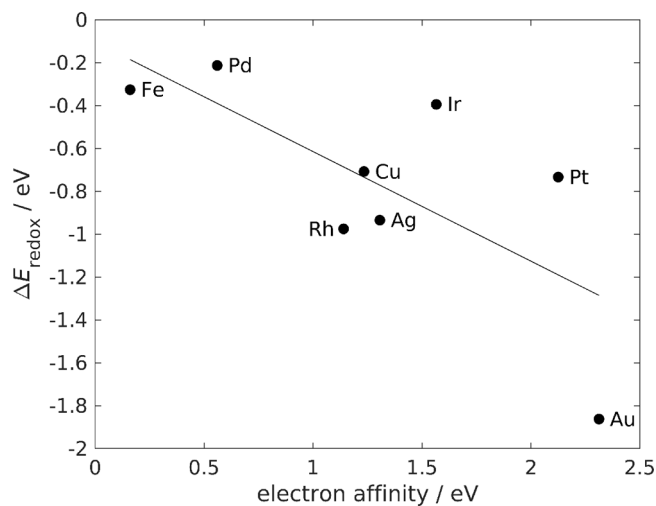


**Figure 9.** Correlation between  $\Delta E_{redox}$  and electron affinity ( $R^2 = 0.49$ ).

Cu, Ag, and Au exhibit a decent correlation, whereas Fe, Ir, and Pt deviate. In the case of Fe, the deviation may be explained by the different vacancy binding geometry involving Fe–O bonding. For Ir and Pt, the geometry is similar to the well-correlated metals and the explanation has to be sought from elsewhere. We note that Ir and Pt exhibit the most exothermic reduction energies, which could be related to the deviation. The redox and  $\Delta E_{icov}^d$  components are not necessarily cleanly separated, as the charge of the metal atom may be different on

the charged surface versus in the vacancy. As such,  $\Delta E_{\text{icov}}^{\text{d}}$  may also include some redox energy. Since the redox component is typically the smallest of the three components, these are relatively minor concerns.

**$\Delta E_{\text{icov}}^{\text{d}}$  Component.** In the last term of the cycle,  $\Delta E_{\text{icov}}^{\text{d}}$ , the interaction between the charged metal atom and the oxygen vacancy is considered. The term includes iono-covalent M–Zr and M–O interactions as well as hybridization between the metal and vacancy orbitals. While the redox term is comparatively small for all the studied metal atoms, with Ag and Au being the exceptions,  $\Delta E_{\text{icov}}^{\text{d}}$  obtains large negative values, which vary from one metal to another with Pt and Ir being most exothermic. From Figure 5, we can conclude that the redox term has only a minor role in the adsorption of a metal atom into an oxygen vacancy of  $\text{ZrO}_2$ , while the  $\Delta E_{\text{icov}}$  contributions dominate the adsorption.

It is also notable that  $\Delta E_{\text{icov}}^{\text{p}}$  exhibits a correlation with both  $\Delta E_{\text{ads}}^{\text{d}}$  ( $R^2 = 0.82$ ) and  $\Delta E_{\text{icov}}^{\text{d}}$  ( $R^2 = 0.87$ ). This indicates that the metal–vacancy interaction is qualitatively similar to the metal–oxygen interaction. The similar (low) electron affinity of the surface oxygen and vacancy orbitals has been suggested as a reason for the similarity.<sup>56</sup>

In addition to the thermodynamic considerations discussed above, we considered the orbital interactions between the adsorbed metal atom and the (pristine or defected) surface. As the vacancy orbital is of *s* symmetry, the *s* orbitals of the adsorbed metal atoms are likely relevant in the vacancy bonding. For instance, Pd has an empty *s* orbital and as such there should be no Pauli repulsion between Pd and the vacancy, facilitating a strong metal–vacancy bond. The Cu group metals have  $d^{10}s^1$  occupancies, meaning that the metal atoms are repulsed by the two *s* electrons of the vacancy. In spite of this, Au binds relatively strongly, which may be ascribed to relativistic effects enhancing the *s*–*d* hybridization.<sup>59</sup>

In summary, our results and detailed analysis show that  $\Delta E_{\text{icov}}^{\text{p}}$  and  $\Delta E_{\text{ads}}^{\text{d}}$  exhibit correlations with Bader charges and each other, with  $\Delta E_{\text{icov}}^{\text{p}}$  also correlating with the  $M_{\text{d}}-O_{\text{p}}$  hybridization index. Thus, surface oxygen/vacancy orbital interactions may be considered as the most important contributors to the binding energies, and the trends across metals are similar for the pristine surface and vacancy sites.

## 4. CONCLUSIONS

We have systematically considered the adsorption of 13 different single transition metal atoms on the pristine and defected *m*- $\text{ZrO}_2(\bar{1}11)$  surface, and shown that each metal makes the reduction energy of the surface more exothermic. The reducibility enhancement when the atom enters the vacancy ranges from  $-1.6$  to  $-4.4$  eV. The magnitude of the effect depends on the electronic properties of the metal atom, the metal adsorption site and, to a limited extent, on the metal–vacancy distance. In particular, we found that binding to a two-coordinated surface oxygen completely prevents the reducibility enhancement. It was also shown that a single metal atom can only facilitate the removal of one oxygen atom from the surface.

The reduction energies as well as the metal adsorption energies correlate with the Bader charges on the transition metal atoms, which we ascribe to the TM atoms withdrawing some electron density from surface oxides via covalent bonding, and to variations in the interaction with the vacancy electrons. Applying a hybridization index, originally developed

for clusters, in our solid metal–oxide system, we show that the hybridization of the metal *d* and oxygen *p*, and to some extent zirconium *d*, orbitals is a main contributor to the metal–surface bonding. The metal–surface interaction correlates with the *s*–*d* excitation energy of the metal, as previously found for  $\text{MgO}(001)$ , another irreducible oxide, making the obtained results more widely applicable to enhancing the reducibility of irreducible oxides besides  $\text{ZrO}_2$ . In addition, a thermodynamic cycle was constructed to describe the various metal–surface and metal–vacancy interactions, and especially to analyze the role of charge transfer.

To conclude, our results show that the irreducible zirconia can be made reducible by adsorbed single transition metal atoms, with Ir and Pt being especially effective reducibility enhancers. The main results are expected to generalize over other irreducible oxides as well, and this has been explicitly discussed in the case of  $\text{MgO}$ . In addition, the variable behavior of different TM adsorbates allows a broad range of reducibilities to be accessed, making it possible to rationally tune the properties of the oxide surface. Such enhanced surface reducibility retains the bulk stability while making the catalyst more active for oxidation reactions (e.g., Mars–von Krevlen-type elementary steps) and nonoxidative dehydrogenation of hydrocarbons and also stabilizing single atom catalyst adsorption. By elucidating the effects of adsorbed TM atoms on oxide reducibility, our results help pave the way for activating irreducible oxides in heterogeneous catalyst design.

## ■ ASSOCIATED CONTENT

### Supporting Information

The Supporting Information is available free of charge at <https://pubs.acs.org/doi/10.1021/acs.jpcc.1c08979>.

Gas-phase reference data, constraint-induced gap states, technical details for the linear-response DFT+*U* implementation in GPAW, effects of varying *U* on adsorbed TM properties, projected density of states plots, and analysis between the correlations (PDF)

## ■ AUTHOR INFORMATION

### Corresponding Author

Karoliina Honkala – Department of Chemistry, Nanoscience Center, University of Jyväskylä, FI-40014 Jyväskylä, Finland; [orcid.org/0000-0002-3166-1077](https://orcid.org/0000-0002-3166-1077); Email: [karoliina.honkala@jyu.fi](mailto:karoliina.honkala@jyu.fi)

### Authors

Ville Korpelin – Department of Chemistry, Nanoscience Center, University of Jyväskylä, FI-40014 Jyväskylä, Finland  
Marko M. Melander – Department of Chemistry, Nanoscience Center, University of Jyväskylä, FI-40014 Jyväskylä, Finland; [orcid.org/0000-0001-7111-1603](https://orcid.org/0000-0001-7111-1603)

Complete contact information is available at: <https://pubs.acs.org/doi/10.1021/acs.jpcc.1c08979>

### Notes

The authors declare no competing financial interest.

## ■ ACKNOWLEDGMENTS

The work was supported by the Academy of Finland through Projects 277222 (V.K. and K.H.), 307853 (M.M.M.), and 317739 (M.M.M. and K.H.). The computational resources

were provided by the CSC-IT Center for Science, Espoo, Finland (<https://www.csc.fi/en/>).

## REFERENCES

- (1) Liu, L.; Corma, A. Metal Catalysts for Heterogeneous Catalysis: From Single Atoms to Nanoclusters and Nanoparticles. *Chem. Rev.* **2018**, *118*, 4981–5079.
- (2) Kauppinen, M. M.; Melander, M. M.; Bazhenov, A. S.; Honkala, K. Unraveling the Role of the Rh–ZrO<sub>2</sub> Interface in the Water–Gas-Shift Reaction via a First-Principles Microkinetic Study. *ACS Catal.* **2018**, *8*, 11633–11647.
- (3) Campbell, C. T. The Energetics of Supported Metal Nanoparticles: Relationships to Sintering Rates and Catalytic Activity. *Acc. Chem. Res.* **2013**, *46*, 1712–1719.
- (4) Kauppinen, M. M.; Korpelin, V.; Verma, A. M.; Melander, M. M.; Honkala, K. Escaping scaling relationships for water dissociation at interfacial sites of zirconia-supported Rh and Pt clusters. *J. Chem. Phys.* **2019**, *151*, 164302.
- (5) Green, I. X.; Tang, W.; Neurock, M.; Yates, J. T., Jr. Spectroscopic Observation of Dual Catalytic Sites During Oxidation of CO on a Au/TiO<sub>2</sub> Catalyst. *Science* **2011**, *333*, 736–739.
- (6) Ruiz Puigdollers, A.; Schlexer, P.; Tosoni, S.; Pacchioni, G. Increasing Oxide Reducibility: The Role of Metal/Oxide Interfaces in the Formation of Oxygen Vacancies. *ACS Catal.* **2017**, *7*, 6493–6513.
- (7) Kauppinen, M. M.; Melander, M. M.; Honkala, K. First-principles insight into CO hindered agglomeration of Rh and Pt single atoms on *m*-ZrO<sub>2</sub>. *Catal. Sci. Technol.* **2020**, *10*, 5847–5855.
- (8) Daelman, N.; Hegner, F. S.; Rellan-Pineiro, M.; Capdevila-Cortada, M.; Garcia-Muelas, R.; Lopez, N. Quasi-degenerate states and their dynamics in oxygen deficient reducible metal oxides. *J. Chem. Phys.* **2020**, *152*, 050901.
- (9) Schlexer, P.; Ruiz Puigdollers, A.; Pacchioni, G. Role of Metal/Oxide Interfaces in Enhancing the Local Oxide Reducibility. *Top. Catal.* **2019**, *62*, 1192–1201.
- (10) Otroshchenko, T.; Jiang, G.; Kondratenko, V. A.; Rodemerck, U.; Kondratenko, E. V. Current status and perspectives in oxidative, non-oxidative and CO<sub>2</sub>-mediated dehydrogenation of propane and isobutane over metal oxide catalysts. *Chem. Soc. Rev.* **2021**, *50*, 473–527.
- (11) Zhang, Y.; Zhao, Y.; Otroshchenko, T.; Han, S.; Lund, H.; Rodemerck, U.; Linke, D.; Jiao, H.; Jiang, G.; Kondratenko, E. V. The effect of phase composition and crystallite size on activity and selectivity of ZrO<sub>2</sub> in non-oxidative propane dehydrogenation. *J. Catal.* **2019**, *371*, 313–324.
- (12) Zhang, Y.; Zhao, Y.; Otroshchenko, T.; Lund, H.; Pohl, M.-M.; Rodemerck, U.; Linke, D.; Jiao, H.; Jiang, G.; Kondratenko, E. V. Control of coordinatively unsaturated Zr sites in ZrO<sub>2</sub> for efficient C–H bond activation. *Nat. Commun.* **2018**, *9*, 3794.
- (13) Zhang, Y.; Zhao, Y.; Otroshchenko, T.; Perehodjuk, A.; Kondratenko, V. A.; Bartling, S.; Rodemerck, U.; Linke, D.; Jiao, H.; Jiang, G.; et al. Structure–Activity–Selectivity Relationships in Propane Dehydrogenation over Rh/ZrO<sub>2</sub> Catalysts. *ACS Catal.* **2020**, *10*, 6377–6388.
- (14) Otroshchenko, T.; Sokolov, S.; Stoyanova, M.; Kondratenko, V. A.; Rodemerck, U.; Linke, D.; Kondratenko, E. V. ZrO<sub>2</sub>-Based Alternatives to Conventional Propane Dehydrogenation Catalysts: Active Sites, Design, and Performance. *Angew. Chem., Int. Ed.* **2015**, *54*, 15880–15883.
- (15) Otroshchenko, T. P.; Kondratenko, V. A.; Rodemerck, U.; Linke, D.; Kondratenko, E. V. Non-oxidative dehydrogenation of propane, *n*-butane, and isobutane over bulk ZrO<sub>2</sub>-based catalysts: effect of dopant on the active site and pathways of product formation. *Catal. Sci. Technol.* **2017**, *7*, 4499–4510.
- (16) Puigdollers, A. R.; Pacchioni, G. CO Oxidation on Au Nanoparticles Supported on ZrO<sub>2</sub>: Role of Metal/Oxide Interface and Oxide Reducibility. *ChemCatChem.* **2017**, *9*, 1119–1127.
- (17) Bazhenov, A. S.; Kauppinen, M. M.; Honkala, K. DFT Prediction of Enhanced Reducibility of Monoclinic Zirconia upon Rhodium Deposition. *J. Phys. Chem. C* **2018**, *122*, 6774–6778.
- (18) Qin, R.; Liu, P.; Fu, G.; Zheng, N. Strategies for Stabilizing Atomically Dispersed Metal Catalysts. *Small Methods* **2018**, *2*, 1700286.
- (19) Liu, J. Catalysis by Supported Single Metal Atoms. *ACS Catal.* **2017**, *7*, 34–59.
- (20) Mortensen, J. J.; Hansen, L. B.; Jacobsen, K. W. Real-space grid implementation of the projector augmented wave method. *Phys. Rev. B* **2005**, *71*, 035109.
- (21) Enkovaara, J.; Rostgaard, C.; Mortensen, J. J.; Chen, J.; Dułak, M.; Ferrighi, L.; Gavnholt, J.; Glinsvad, C.; Haikola, V.; Hansen, H. A.; et al. Electronic structure calculations with GPAW: a real-space implementation of the projector augmented-wave method. *J. Phys.: Condens. Matter* **2010**, *22*, 253202.
- (22) Larsen, A. H.; Mortensen, J. J.; Blomqvist, J.; Castelli, I. E.; Christensen, R.; Dułak, M.; Friis, J.; Groves, M. N.; Hammer, B.; Hargus, C.; et al. The atomic simulation environment—a Python library for working with atoms. *J. Phys.: Condens. Matter* **2017**, *29*, 273002.
- (23) Bahn, S. R.; Jacobsen, K. W. An object-oriented scripting interface to a legacy electronic structure code. *Comput. Sci. Eng.* **2002**, *4*, 56–66.
- (24) Perdew, J. P.; Burke, K.; Ernzerhof, M. Generalized Gradient Approximation Made Simple. *Phys. Rev. Lett.* **1996**, *77*, 3865–3868.
- (25) Perdew, J. P.; Burke, K.; Ernzerhof, M. Generalized Gradient Approximation Made Simple [Phys. Rev. Lett. *77*, 3865 (1996)]. *Phys. Rev. Lett.* **1997**, *78*, 1396–1396.
- (26) Blöchl, P. E. Projector augmented-wave method. *Phys. Rev. B* **1994**, *50*, 17953–17979.
- (27) Bazhenov, A. S.; Honkala, K. Understanding Structure and Stability of Monoclinic Zirconia Surfaces from First-Principles Calculations. *Top. Catal.* **2017**, *60*, 382–391.
- (28) Sansonetti, J.; Martin, W.; Young, S. *Handbook of Basic Atomic Spectroscopic Data (version 1.1.2)*; National Institute of Standards and Technology: Gaithersburg, MD, 2005; [Online] Available: <http://physics.nist.gov/Handbook> [2021, August 17].
- (29) Himmethoglu, B.; Floris, A.; de Gironcoli, S.; Cococcioni, M. Hubbard-corrected DFT energy functionals: The LDA+U description of correlated systems. *Int. J. Quantum Chem.* **2014**, *114*, 14–49.
- (30) Syzgantseva, O. A.; Calatayud, M.; Minot, C. Revealing the Surface Reactivity of Zirconia by Periodic DFT Calculations. *J. Phys. Chem. C* **2012**, *116*, 6636–6644.
- (31) Chen, H.-Y. T.; Tosoni, S.; Pacchioni, G. Hydrogen Adsorption, Dissociation, and Spillover on Ru<sub>10</sub> Clusters Supported on Anatase TiO<sub>2</sub> and Tetragonal ZrO<sub>2</sub> (101) Surfaces. *ACS Catal.* **2015**, *5*, 5486–5495.
- (32) Lutfalla, S.; Shapovalov, V.; Bell, A. T. Calibration of the DFT/GGA+U Method for Determination of Reduction Energies for Transition and Rare Earth Metal Oxides of Ti, V, Mo, and Ce. *J. Chem. Theory Comput.* **2011**, *7*, 2218–2223.
- (33) Cococcioni, M.; de Gironcoli, S. Linear response approach to the calculation of the effective interaction parameters in the LDA + U method. *Phys. Rev. B* **2005**, *71*, 035105.
- (34) Kulik, H. J.; Cococcioni, M.; Scherlis, D. A.; Marzari, N. Density Functional Theory in Transition-Metal Chemistry: A Self-Consistent Hubbard U Approach. *Phys. Rev. Lett.* **2006**, *97*, 103001.
- (35) Dudarev, S. L.; Botton, G. A.; Savrasov, S. Y.; Humphreys, C. J.; Sutton, A. P. Electron-energy-loss spectra and the structural stability of nickel oxide: An LSDA+U study. *Phys. Rev. B* **1998**, *57*, 1505–1509.
- (36) Park, S.-G.; Magyari-Köpe, B.; Nishi, Y. Electronic correlation effects in reduced rutile TiO<sub>2</sub> within the LDA + U method. *Phys. Rev. B* **2010**, *82*, 115109.
- (37) Plata, J. J.; Márquez, A. M.; Sanz, J. F. Communication: Improving the density functional theory+U description of CeO<sub>2</sub> by including the contribution of the O 2*p* electrons. *J. Chem. Phys.* **2012**, *136*, 041101.
- (38) Huang, X.; Ramadugu, S. K.; Mason, S. E. Surface-Specific DFT + U Approach Applied to  $\alpha$ -Fe<sub>2</sub>O<sub>3</sub> (0001). *J. Phys. Chem. C* **2016**, *120*, 4919–4930.

- (39) Brown, J. J.; Page, A. J. The Hubbard-U correction and optical properties of d0 metal oxide photocatalysts. *J. Chem. Phys.* **2020**, *153*, 224116.
- (40) Hsu, H.; Umamoto, K.; Cococcioni, M.; Wentzcovitch, R. First-principles study for low-spin LaCoO<sub>3</sub> with a structurally consistent Hubbard U. *Phys. Rev. B* **2009**, *79*, 125124.
- (41) Zhao, Q.; Kulik, H. J. Stable Surfaces That Bind Too Tightly: Can Range-Separated Hybrids or DFT+U Improve Paradoxical Descriptions of Surface Chemistry? *J. Phys. Chem. Lett.* **2019**, *10*, 5090–5098.
- (42) Perdew, J. P.; Levy, M. Physical Content of the Exact Kohn-Sham Orbital Energies: Band Gaps and Derivative Discontinuities. *Phys. Rev. Lett.* **1983**, *51*, 1884–1887.
- (43) Çakır, D.; Gülsiren, O. Adsorption of Pt and Bimetallic PtAu Clusters on the Partially Reduced Rutile (110) TiO<sub>2</sub> Surface: A First-Principles Study. *J. Phys. Chem. C* **2012**, *116*, 5735–5746.
- (44) French, R. H.; Glass, S. J.; Ohuchi, F. S.; Xu, Y. N.; Ching, W. Y. Experimental and theoretical determination of the electronic structure and optical properties of three phases of ZrO<sub>2</sub>. *Phys. Rev. B* **1994**, *49*, 5133–5142.
- (45) McComb, D. W. Bonding and electronic structure in zirconia pseudopolymorphs investigated by electron energy-loss spectroscopy. *Phys. Rev. B* **1996**, *54*, 7094–7102.
- (46) Dash, L. K.; Vast, N.; Baranek, P.; Cheynet, M.-C.; Reining, L. Electronic structure and electron energy-loss spectroscopy of ZrO<sub>2</sub> zirconia. *Phys. Rev. B* **2004**, *70*, 245116.
- (47) Teeparthi, S.; Awın, E.; Kumar, R. Dominating role of crystal structure over defect chemistry in black and white zirconia on visible light photocatalytic activity. *Sci. Rep.* **2018**, *8*, 5541.
- (48) Jiang, N.; Spence, J. C. Valence electron energy-loss spectroscopy study of ZrSiO<sub>4</sub> and ZrO<sub>2</sub>. *Ultramicroscopy* **2013**, *134*, 68–76.
- (49) Hammer, B.; Hansen, L. B.; Nørskov, J. K. Improved adsorption energetics within density-functional theory using revised Perdew-Burke-Ernzerhof functionals. *Phys. Rev. B* **1999**, *59*, 7413–7421.
- (50) Klüpfel, S.; Klüpfel, P.; Jónsson, H. The effect of the Perdew-Zunger self-interaction correction to density functionals on the energetics of small molecules. *J. Chem. Phys.* **2012**, *137*, 124102.
- (51) Tang, W.; Sanville, E.; Henkelman, G. A grid-based Bader analysis algorithm without lattice bias. *J. Phys.: Condens. Matter* **2009**, *21*, 084204.
- (52) Häkkinen, H.; Moseler, M.; Landman, U. Bonding in Cu, Ag, and Au Clusters: Relativistic Effects, Trends, and Surprises. *Phys. Rev. Lett.* **2002**, *89*, 033401.
- (53) Cordero, B.; Gómez, V.; Platero-Prats, A. E.; Revés, M.; Echeverría, J.; Cremades, E.; Barragán, F.; Alvarez, S. Covalent radii revisited. *Dalton Trans* **2008**, 2832–2838.
- (54) Shannon, R. D. Revised effective ionic radii and systematic studies of interatomic distances in halides and chalcogenides. *Acta Crystallogr. A* **1976**, *32*, 751–767.
- (55) Yudanov, I.; Pacchioni, G.; Neyman, K.; Rösch, N. Systematic Density Functional Study of the Adsorption of Transition Metal Atoms on the MgO(001) Surface. *J. Phys. Chem. B* **1997**, *101*, 2786–2792.
- (56) Matveev, A. V.; Neyman, K. M.; Yudanov, I. V.; Rösch, N. Adsorption of transition metal atoms on oxygen vacancies and regular sites of the MgO(001) surface. *Surf. Sci.* **1999**, *426*, 123–139.
- (57) Markovits, A.; Paniagua, J. C.; López, N.; Minot, C.; Illas, F. Adsorption energy and spin state of first-row transition metals adsorbed on MgO(100). *Phys. Rev. B* **2003**, *67*, 115417.
- (58) Neyman, K.; Inntam, C.; Nasluzov, V.; Kosarev, R.; Rösch, N. Adsorption of d-metal atoms on the regular MgO(001) surface: Density functional study of cluster models embedded in an elastic polarizable environment. *Appl. Phys. A: Mater. Sci. Process.* **2004**, *78*, 823–828.
- (59) Neyman, K. M.; Inntam, C.; Matveev, A. V.; Nasluzov, V. A.; Rösch, N. Single d-Metal Atoms on F<sub>s</sub> and F<sub>i</sub> Defects of MgO(001): A Theoretical Study across the Periodic Table. *J. Am. Chem. Soc.* **2005**, *127*, 11652–11660.
- (60) Jung, C.; Ishimoto, R.; Tsuboi, H.; Koyama, M.; Endou, A.; Kubo, M.; Del Carpio, C. A.; Miyamoto, A. Interfacial properties of ZrO<sub>2</sub> supported precious metal catalysts: A density functional study. *Appl. Catal., A* **2006**, *305*, 102–109.
- (61) Helali, Z.; Markovits, A.; Minot, C.; Abderrabba, M. First-row transition metal atoms adsorption on rutile TiO<sub>2</sub>(110) surface. *Struct. Chem.* **2012**, *23*, 1309–1321.
- (62) Helali, Z.; Markovits, A.; Minot, C.; Abderrabba, M. Metal atom adsorption on a defective TiO<sub>2</sub>-<sub>x</sub> support. *Chem. Phys. Lett.* **2014**, *594*, 23–29.
- (63) Grau-Crespo, R.; Hernández, N. C.; Sanz, J. F.; de Leeuw, N. H. Theoretical Investigation of the Deposition of Cu, Ag, and Au Atoms on the ZrO<sub>2</sub>(111) Surface. *J. Phys. Chem. C* **2007**, *111*, 10448–10454.
- (64) Ganduglia-Pirovano, M. V.; Hofmann, A.; Sauer, J. Oxygen vacancies in transition metal and rare earth oxides: Current state of understanding and remaining challenges. *Surf. Sci. Rep.* **2007**, *62*, 219–270.
- (65) Pacchioni, G. Electronic interactions and charge transfers of metal atoms and clusters on oxide surfaces. *Phys. Chem. Chem. Phys.* **2013**, *15*, 1737–1757.
- (66) Dalverny, A.-L.; Filhol, J.-S.; Lemoigno, F.; Doublet, M.-L. Interplay between Magnetic and Orbital Ordering in the Strongly Correlated Cobalt Oxide: A DFT + U Study. *J. Phys. Chem. C* **2010**, *114*, 21750–21756.
- (67) Singh, V.; Kosa, M.; Majhi, K.; Major, D. T. Putting DFT to the Test: A First-Principles Study of Electronic, Magnetic, and Optical Properties of Co<sub>3</sub>O<sub>4</sub>. *J. Chem. Theory Comput.* **2015**, *11*, 64–72.
- (68) Andersin, J.; Nevalaita, J.; Honkala, K.; Häkkinen, H. The Redox Chemistry of Gold with High-Valence Doped Calcium Oxide. *Angew. Chem., Int. Ed.* **2013**, *52*, 1424–1427.
- (69) Mehta, P.; Greeley, J.; Delgass, W. N.; Schneider, W. F. Adsorption Energy Correlations at the Metal–Support Boundary. *ACS Catal.* **2017**, *7*, 4707–4715.
- (70) Song, W.; Martsinovich, N.; Heckl, W. M.; Lackinger, M. Born–Haber Cycle for Monolayer Self-Assembly at the Liquid–Solid Interface: Assessing the Enthalpic Driving Force. *J. Am. Chem. Soc.* **2013**, *135*, 14854–14862.
- (71) Lany, S.; Zunger, A. Accurate prediction of defect properties in density functional supercell calculations. *Modell. Simul. Mater. Sci. Eng.* **2009**, *17*, 084002.
- (72) Wang, Y.; Florez, E.; Mondragon, F.; Truong, T. N. Effects of metal–support interactions on the electronic structures of metal atoms adsorbed on the perfect and defective MgO(100) surfaces. *Surf. Sci.* **2006**, *600*, 1703–1713.
- (73) Chaves, A. S.; Rondina, G. G.; Piotrowski, M. J.; Tereshchuk, P.; Da Silva, J. L. F. The Role of Charge States in the Atomic Structure of Cu<sub>n</sub> and Pt<sub>n</sub> (n = 2–14 atoms) Clusters: A DFT Investigation. *J. Phys. Chem. A* **2014**, *118*, 10813–10821.
- (74) Raab, J.; Roos, B. O. Excitation Energies for Transition Metal Atoms – A Comparison between Coupled Cluster Methods and Second-Order Perturbation Theory. In *Adv. Quantum Chem.*; Academic Press: New York, 2005; Vol. 48, pp 421–433.